Shock-induced polymorphic transitions of PbF$_2$ up to 1 TPa and their implications for the universal behavior of shocked AX_2 compounds

Xun Liu,[1,2] Chang Gao,[1] Tsutomu Mashimo,[2] Norimasa Ozaki ●,[3,*] Williams J. Nellis ●,[4] Gang Yang ●,[1]
Haijun Huang,[1,†] Shintaro Morioka,[3] Kohei Miyanishi,[5] Takayoshi Sano ●,[5] and Ryosuke Kodama[3,5]

[1]*School of Science, Wuhan University of Technology, Wuhan, Hubei 430070, China*

[2]*Institute of Pulsed Power Science, Kumamoto University, Kurokami, Kumamoto 860–8555, Japan*

[3]*Graduate School of Engineering, Osaka University, Suita, Osaka 565–0871, Japan*

[4]*Department of Physics, Harvard University, Cambridge, Massachusetts 02138, USA*

[5]*Institute of Laser Engineering, Osaka University, Suita, Osaka 565–0871, Japan*

Hugoniot data for PbF$_2$ single crystals were measured for pressures up to 1 TPa through gas gun and laser shock experiments. Experimental results show that PbF$_2$ transforms to a less compressible phase at 29 GPa and possibly melts at 57 GPa. Quantum molecular-dynamics simulations were also performed to calculated the liquid Hugoniot for PbF$_2$. The simulated results are in good agreement with the experimental results, supporting the high-pressure phase is liquid. The current study, combined with previous studies on TiO$_2$, SiO$_2$, and CaF$_2$, suggests that for AX_2 compounds, decreasing of Hugoniot slope can be taken as an indication of melting, and the Hugoniot slope approaches 1.2 at ultrahigh pressure.

I. INTRODUCTION

Lead fluoride (PbF$_2$) is a technologically important scintillation material, which has also attracted considerable attention owing to its strong superionic character [1–3]. As a typical AX_2 compound, where A and X represent a divalent cation and halogen atom, or a tetravalent cation and oxygen atom, respectively, the phase-transition sequence of PbF$_2$ under static high pressures has been widely studied [4–7]. The phase transition of difluorides exhibits a systematic dependence on cation radius and pressure; the larger the cation radius, the lower the transition pressure to a specific structure [8]. Under ambient conditions, PbF$_2$ crystallizes in a cubic fluorite structure (β phase, space group: $Fm\bar{3}m$) with a cation coordination number (CN) = 8. At 0.4 GPa, it transforms into an orthorhombic cotunnite structure (α phase, space group: $Pnma$) with CN = 9. The α phase is metastable at zero pressure for temperatures less than 610 K [9].

Difluorides are also considered as good analogs for the high-pressure behavior of SiO$_2$ owing to their low transition pressures. First-principles simulations predict that SiO$_2$ adopts the cotunnite structure at pressures greater than ∼700 GPa, which corresponds to the conditions of a super-Earth's deep interior [10]. Numerous metal oxides such as TiO$_2$, SnO$_2$, PbO$_2$, ZrO$_2$, HfO$_2$, CeO$_2$, and TeO$_2$ also adopt the cotunnite structure under high pressure [11–17]. A theoretical study predicts that the postcotunnite phase of PbF$_2$ adopts the hexagonal Ni$_2$In-type structure (space group: $P6_3/mmc$, $CN = 11$), similar to that of CaF$_2$, BaF$_2$, and SrF$_2$ [6].

However, the Ni$_2$In-type phase was not observed experimentally until a recent work by Stan *et al.*, where they found that temperature has a crucial role in phase transition [7]. The Ni$_2$In-type phase can only be observed under conditions of high pressure and temperature. At room temperature, PbF$_2$ transforms into an isosymmetric Co$_2$Si-type structure (γ phase, space group: $Pnam$, $CN = 11$) in the range of 10–22 GPa; this structure is stable up to at least 75 GPa [5,7].

Shock compression is a unique approach to realize both high pressure and high temperature. The relatively large radius of the Pb^{2+} ion and high density (resulting in high shock impedance) of PbF$_2$ make it an acceptable candidate for studying the phase transition of AX_2 compounds. In this study, we performed Hugoniot measurements on PbF$_2$ up to ∼1 TPa. The elastic-plastic transition, phase transition, and equation of state of PbF$_2$ were studied. Quantum molecular-dynamics (QMD) simulations were also performed for comparison with experimental results.

II. EXPERIMENTAL METHODS

Initially transparent, plate-shaped β-PbF$_2$ single crystals with purity greater than 99.9% were supplied by Shenzhen Hongyu Technology Co., Ltd. The density of the samples was measured to be 7.740 ± 0.004 g/cm^3 using the Archimedes method. The sample sizes were roughly $12 \times 15 \times 2.5$ mm. Both surfaces of the samples were polished in an optical furnace and made parallel within 2 μm over the entire area. The crystal directions were identified by x-ray Laue diffraction. The basic properties of the samples are listed in Table I.

The Hugoniot data of PbF$_2$ were measured using three different methods. Shots No. 1–4 were measured by the inclined-mirror method [20] combined with a key-powder gun

*norimasa.ozaki@eie.eng.osaka-u.ac.jp

†hjhuang@whut.edu.cn

TABLE I. Ultrasonic data and thermodynamic parameters of PbF$_2$ at ambient conditions.

Properties	Quantities
Density[a]	7.740 g/cm^3
Longitudinal sound velocity c_l[b]	3.513 km/s [100]
	3.422 km/s [111]
Transverse sound velocity c_t[b]	1.636 km/s [100]
	1.728 km/s [111]
Buck sound velocity C_b[c]	2.854 km/s
Bulk modulus K_0[c]	63.5 GPa
Thermal expansion coefficient α[d]	28.5×10^{-6} K^{-1}
Specific heat C_v[b]	77.0 J/(mol K)
Debye temperature[b]	200 K
Grüneisen parameter[b]	2.3

[a]Measured using Archimedes' method.
[b]Reference [18].
[c]Calculated from the elastic constants in Ref. [18].
[d]Reference [19].

[21] at Kumamoto University. The experimental configuration is displayed in Fig. 1(a). The measurements were performed using a rotating mirror-type streak camera with a maximum writing speed greater than 10 mm/μs and a high-intensity pulsed dye laser. The time resolution was greater than 1 ns using a 2-mm-wide slit. The tilt angles of the shock wave in the direction parallel and normal to the slit were determined by the streak photograph and two electrical pins, respectively. Details regarding the inclined-mirror method and data analysis procedures can be found in our previous studies [20,22]. A typical inclined-mirror experimental photograph (shot No. 3) is displayed in Fig. 1(a). It indicates a two-wave structure. The first shock wave arrives at the front surface of the diver plate and specimen at t_0 and t_1 respectively. The kink at t_2 is due to the arrival of the second shock wave. For shock stress greater than 35 GPa, a single shock wave was observed.

At higher shock pressures (shots No. 5–9), the Hugoniot data were measured by a displacement interferometer system for any reflector (DISAR) [23] combined with a two-stage light gas gun [24] at Wuhan University of Technology. The experimental configuration is displayed in Fig. 1(b). The backing surfaces of the samples were vapor deposited with ~100-nm copper films to reflect the laser. The driver/sample interface and free-surface motions were monitored by a DISAR with a time resolution of 100 ps. Three electrical pins were mounted uniformly on the drive plate to determine the incline angle of the shock wave. Typical optical fringe patterns (shot No. 6) recorded by DISAR and the deduced particle velocities are displayed in Fig. 1(b). When a shock wave arrives at the driver/sample interface (t_1), several fringes are generated; however, they soon become indistinct owing to the loss of transparency in PbF$_2$. The fringes appear again at t_2 when the shock wave arrives at the free surface of the sample. The shock velocities (U_S) can thus be simply calculated by $U_S = \frac{H}{(t_2 - t_1)}$, where H is the sample thickness. In the above gun experiments, flyer velocities were measured by the electromagnetic method with an accuracy that is typically within 0.5%. We used copper (Cu), tantalum (Ta), and tungsten (W)
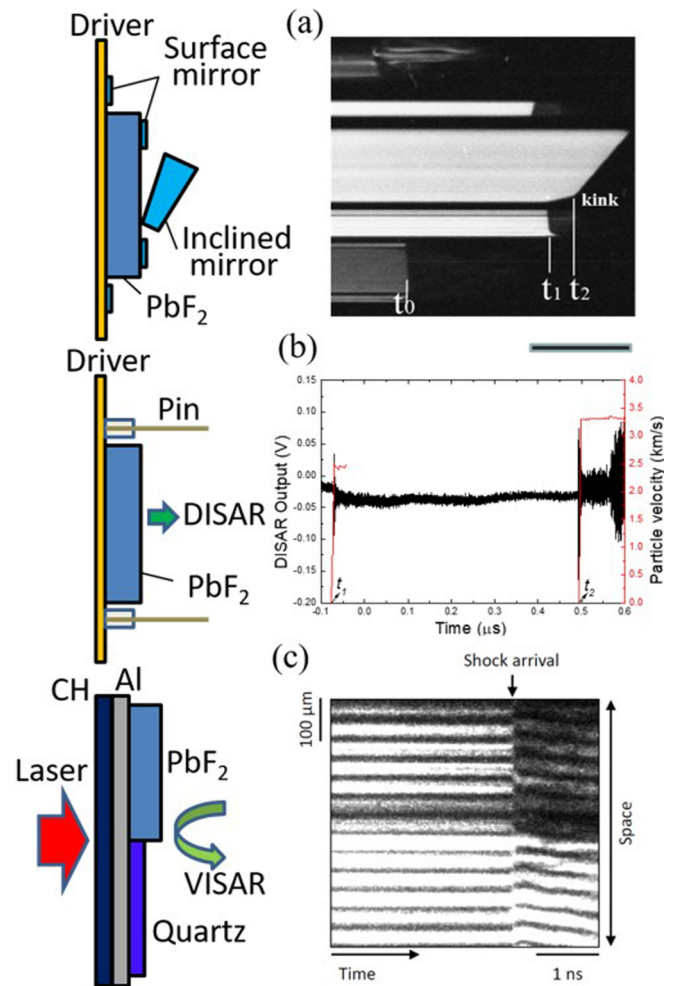

FIG. 1. Experimental configurations and typical results: (a) inclined-mirror method (No. 3), (b) DISAR method (No. 6), and (c) laser shock (No. 12).

as the flyer and driver plates; their Hugoniot parameters are listed in Table II.

Three laser shock experiments (Shots No. 10–12) were performed on the GXII laser system at Osaka University [26,27] with final shock pressures of approximately 300 and 960 GPa. The experimental configuration is displayed in Fig. 1(c) with a typical velocity interferometer system for any reflector (VISAR) image. Because both quartz and PbF$_2$ become optically reflective at pressures greater than ~100 GPa, the shock velocities of these were measured directly by the VISARs [28]. Once the shockwave velocities were measured, the corresponding particle velocities (U_P)

TABLE II. Hugoniot parameters of flyer and driver plates.

Material	$b_0(g/cm^3)$[a]	$C_0(km/s)$[b]	S[b]
Cu [25]	8.935	3.933	1.500
Ta [25]	16.654	3.293	1.307
W [22]	19.23	4.137	1.242

[a]ρ_0 is the density at ambient conditions.
[b]C_0 and S are parameters of U_s and U_p relationship: $U_s = C_0 + S U_p$.

TABLE III. Hugoniot data of PbF_2. U_p, U_s, ρ, and P are the particle velocity, shock velocity, density, and Hugoniot pressure, respectively.

No.	Method	Axis	Flyer/ driver	Flyer speed (km/s)	U_p (km/s)	U_s (km/s)	ρ (g/cm^3)	P (GPa)	Tilt angle (°)
1	IM[a]	111	Cu/Cu	1.187(7)	0.15(1)	3.63(1)	8.08(3)	4.3(2)	0.7
					0.75(1)	3.05(1)	10.16(5)	18.1(3)	
2	IM[a]	111	W/W	1.182(6)	0.17(1)	3.63(2)	8.12(3)	4.7(3)	1.0
					0.91(1)	3.27(1)	10.67(5)	23.4(3)	
3	IM[a]	111	W/W	1.416(7)	0.18(1)	3.64(1)	8.14(3)	5.0(2)	1.8
					1.08(1)	3.50(1)	11.17(5)	29.4(3)	
4	IM[a]	111	W/W	1.600(8)	1.20(1)	3.79(2)	11.33(5)	35.3(4)	1.5
5	DISAR[b]	111	Cu/Cu	2.380(12)	1.41(1)	4.20(1)	11.69(6)	46.1(5)	
6	DISAR	100	Cu/Cu	2.707(14)	1.59(2)	4.56(1)	11.87(8)	56.1(7)	1.2
7	DISAR	100	Ta/Ta	2.963(15)	1.96(2)	5.08(1)	12.59(8)	77.1(8)	1.6
8	DISAR	111	Ta/Ta	3.659(18)	2.39(2)	5.69(1)	13.32(8)	105.2(9)	1.9
9	DISAR	111	Ta/Ta	4.428(22)	2.85(3)	6.41(2)	13.93(12)	141.2(16)	1.1
10	Laser Shock	100	None/Al		4.51(9)	8.60(12)	16.28(44)	300.2(73)	
11	Laser Shock	100	None/Al		4.52(9)	8.66(12)	16.19(43)	303.0(74)	
12	Laser Shock	100	None/Al		9.11(11)	13.66(12)	23.24(69)	963.0(144)	

[a]Inclined-mirror method.
[b]One of the three pin signals failed.

were determined by matching the impedance between driver and sample plates [29]. We first determined the shock state in quartz with the measured quartz Us and the known quartz Hugoniot; $U_s = 5.477 + 1.242U_P - 2.453U_P^2 e^{-0.4336U_P}$ [30]. The Hugoniot state in Al driver was then calculated from the shocked quartz state, the Al Hugoniot, and its release adiabat. The Al Hugoniot; $U_s = 6.322 + 1.189U_P$ and the release model developed by Knudson were used [31]. To perform the impedance matching analysis between Al and PbF_2, the reshock Hugoniot of Al was calculated based on the Mie-Grüneisen equation of states (EOS) theory;

$$P_2' = \frac{P_2 - \frac{1}{2}\left(\frac{\gamma}{V}\right)_2 (P_2 - P_1)(V_0 - V_2)}{1 - \frac{1}{2}\left(\frac{\gamma}{V}\right)_2 (V_1 - V_2)}, \quad (1)$$

where $V_0 = 1/\rho_0$ is the specific volume at zero pressure, subscript 1 refers to the initial shock state, P_2 and P_2' is the shock and reshock pressures at volume V_2, respectively. In Eq. (1), the Grüneisen parameter of Al has the form $\gamma/V = \gamma_0/V_0$ with $\gamma_0 = 2.14$ [32]. Although different diagnostic methods were used in our experiments, the effectiveness of these methods has been proven in previous studies [22,27,33].

III. QUANTUM MOLECULAR-DYNAMICS SIMULATIONS

To further explore the properties of PbF_2 under shock compression, we calculated the Hugoniot of PbF_2 in its liquid phase by QMD using QUANTUM ESPRESSO [34]. The Hugoniot data were determined by the Rankine-Hugoniot relation

$$E - E_0 = \frac{1}{2}(P + P_0)(V_0 - V), \quad (2)$$

where E is the specific internal energy, P is the pressure, and $V = 1/\rho$ is the specific volume. The subscript 0 denotes the reference state. Every Hugoniot point for PbF_2 was solved with the second-order Newton's polynomial interpolation by several EOS points with the same temperature and different densities. All the calculations were performed in a periodic cubic box containing 48 atoms, which has been found to be

sufficient for the EOS simulation [35]. For a given temperature and density, the time step to move the ions was determined by a scaling formula that was 1/40 of the distance of the average atoms divided by the average thermal velocity, and ranged from 0.1 to 1 fs. The trajectories of the last 3000 steps were used to statistically calculate the required physical properties after the system had achieved thermal equilibrium for the first 3000 steps, which made the numerical error of the total energy and presksure less than 1%. The Perdew-Burke-Ernzerhof [36] parametrization of the generalized gradient approximation [37] to the exchange–correlation interaction was employed. The optimized norm-conserving Vanderbilt pseudopotentials [38] (with 7 and 14 valence electrons for F and Pb, respectively) for QUANTUM ESPRESSO in UPF format were used with a kinetic energy cutoff of 100 Ry. A shifted $2 \times 2 \times 2$ Monkhorst–Pack k-points grid was meshed to sample the Brillouin zone. The mean-square displacements were calculated after each MD run to confirm that the structures were in a liquid phase.

IV. RESULTS AND DISCUSSIONS

A. Phase transitions of PbF_2 under shock compression

The measured PbF_2 Hugoniot data are summarized in Table III and plotted in Fig. 2. It can be clearly observed that the PbF_2 Hugoniot data can be divided into four regions; an elastic region for $0 < U_P < 0.2$ km/s, a low-pressure (LP) phase region for $0.6 < U_P < 1.1$ km/s, an intermediate (IM) phase region for $1.1 < U_P < 1.6$ km/s, and a high-pressure (HP) phase region for $U_P > 1.6$ km/s. From the linear fits to the Hugoniot data, the values of $U_S = 2.00(2) + 1.41(2)U_P$ and $U_S = 2.22(6) + 1.46(2)U_P$ were obtained for the LP and HP phases, respectively. For shots No. 1–3, the inclined mirror results indicate two-wave structures. The wave interactions can influence the determination of the shock velocities, and in turn, the presence of the phase transition. We corrected the shock velocities following the method presented in
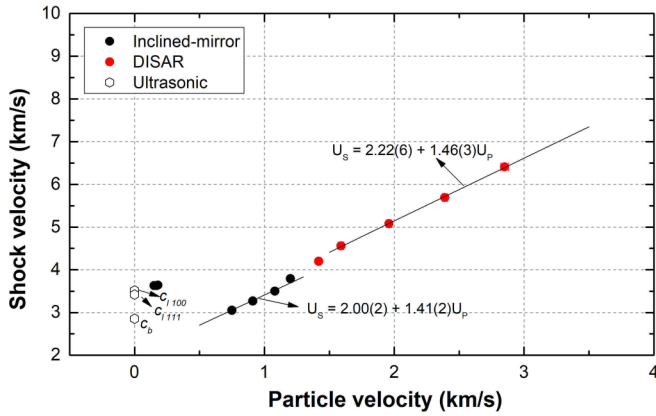
FIG. 2. Shock velocity (U_S)-particle velocity (U_p) relation for PbF$_2$. c_b is the bulk sound velocity, and c_{l100} and c_{l111} are the longitudinal sound velocities along the $\langle 100 \rangle$ and $\langle 111 \rangle$ directions, respectively. The solid lines are linear fittings to the Hugoniot data.

previous studies and described in Appendix A. After correction, the shock velocities decreased marginally, whereas the particle velocities changed minimally. Therefore, the existence of the phase transition was not influenced by the data analysis method.

The pressures and densities at the shock state were calculated from the Hugoniot data with the Rankine-Hugoniot conservation equations [31]. The shock compression curve (pressure-density) of PbF$_2$ is plotted in Fig. 3, with the room-temperature static compression data measured by Stan *et al.* [7]. The Hugoniot elastic limits (HELs) of PbF$_2$ for shocks along the $\langle 111 \rangle$ directions were measured to be 4.3–5.0 GPa; the HEL increased with the driving force, similar to some other ceramics [39]. At room temperature, β-PbF$_2$ transforms
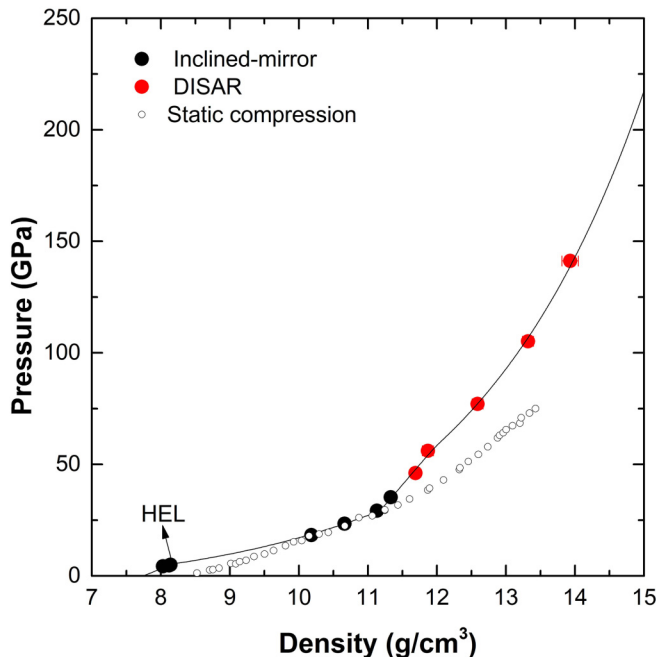

FIG. 3. Hugoniot compression curve of PbF$_2$ with static compression data (Ref. [7]).
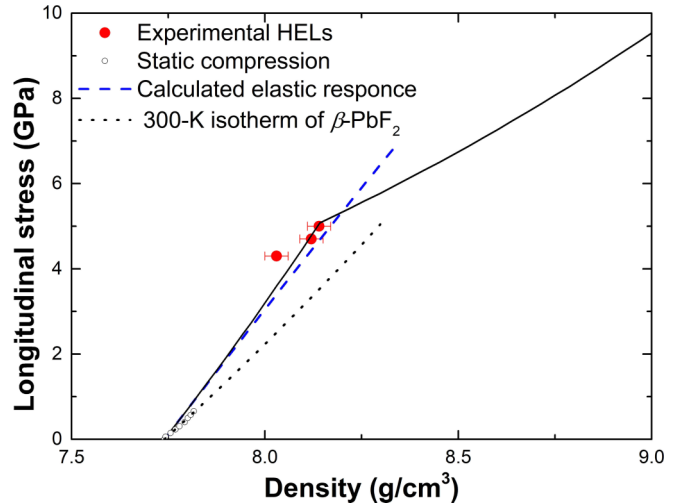

FIG. 4. Comparing Hugoniot curve with calculated elastic response and static compression data of β-PbF$_2$ (Ref. [39]). The dotted line is a third-order Birch-Murnaghan fitting to the static compression data.

to α-PbF$_2$ at 0.4 GPa [9]; this transition pressure is considerably less than the HEL determined herein. It is possible that the aforementioned HEL was not caused by the elastic-plastic transition; rather, it could have been the $\beta \rightarrow \alpha$ phase transition. To identify its property, we calculated the elastic shock response of PbF$_2$ based on the nonlinear elastic theory (see Appendix B); the results are displayed in Fig. 4. For pressures less than 5.0 GPa, the Hugoniot compression curve is close to the calculated elastic response and clearly deviates from the 300 K isotherm of β-PbF$_2$, supporting the fact that PbF$_2$ is in the elastic region. With increasing pressure, the Hugoniot compression data are consistent with the static data, except for the different initial densities of the sample. We started with β-PbF$_2$ with an initial density of 7.740 g/cm^3, whereas the static compression study started from α-PbF$_2$ with an initial density of $\sim$8.450 g/cm^3 [7]. It is likely that β-PbF$_2$ enters the α phase directly from the elastic state and does not induce a phase-transition wave, similar to the wurtzite-rocksalt structure transition observed on shocked CdS [40]. Stan *et al.* also observed a continuous isosymmetric phase transition to a postcotunnite Co$_2$Si-type structure in the range 10–22 GPa [7]. The measured Hugoniot densities in the LP region are consistent with both the α or postcotunnite structures and the present data cannot distinguish between these possible phases or other unknown phases.

The Hugoniot compression curve indicates a phase transition at $\sim$29 GPa, as indicated in Fig. 5. The shock temperature at 29 GPa was estimated to be 880 K from thermodynamic calculations. Under static compression, PbF$_2$ partially transformed to a Ni$_2$In-type structure phase at or greater than 25.9 GPa with heating greater than 1200 K [7]. Considering the similar transition pressure-temperature under dynamic and static compressions, the IM phase (29–57 GPa) observed here may adopt the Ni$_2$In-type structure. However, as the current continuum data cannot provide a direct evidence, the nature of the IM phase needs further study. The isotherms of 0 K (calculated theoretically) and 300 K
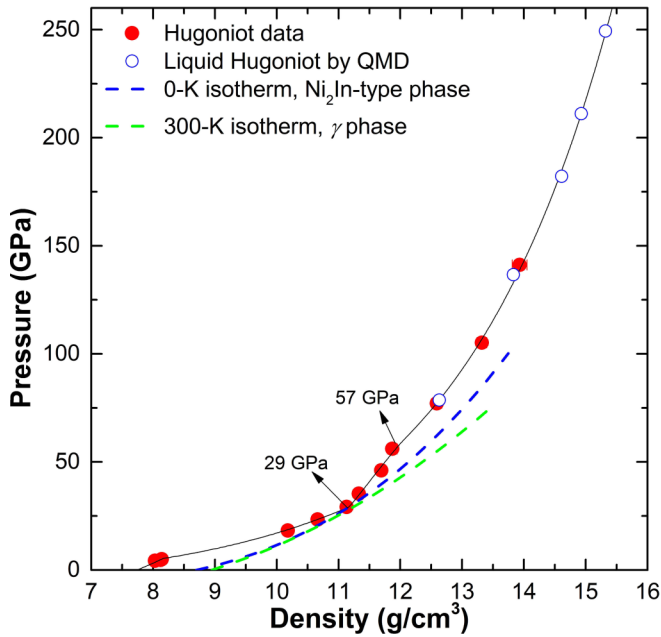
FIG. 5. Hugoniot curve of PbF_2 with QMD results. The blue and green lines are calculated 0–K (Ref. [6]) and experimentally determined 300 K (Ref. [7]) isotherms of the Ni_2In type and γ-phase PbF_2, respectively. The black line is the Hugoniot compression curve.

(determined experimentally) for the Ni_2In-type and γ-phase PbF_2 were also plotted in Fig. 5 for comparison. Beyond 57 GPa, PbF_2 transforms to a more compressible phase. We calculated the liquid Hugoniot of PbF_2 by QMD as described in Sec. III; the results are listed in Table IV and plotted in Fig. 5. The QMD results are in excellent agreement with the experimental results, suggesting that the HP phase is liquid. In one of our laser shock experiments with a pressure of approximately 75 GPa (not shown here), we observed the shock front become reflective, which also indicates that the HP phase is liquid [41].

B. Shock response of PbF_2 at ultrahigh pressure

The shock responses of AX_2 compounds at extremely high pressures have also attracted considerable attention. We measured the Hugoniot of PbF_2 up to ∼1 TPa with the laser facilities at Osaka University. These results, along with our DISAR and QMD results, are plotted in Fig. 6. Only the Hugoniot data in the liquid region are presented for clarity. Similar to the observations on quartz [41] and TiO_2 [35], the Hugoniot of liquid PbF_2 has a notable curvature. A modified

TABLE IV. Hugoniot data of liquid PbF_2 by QMD simulation.

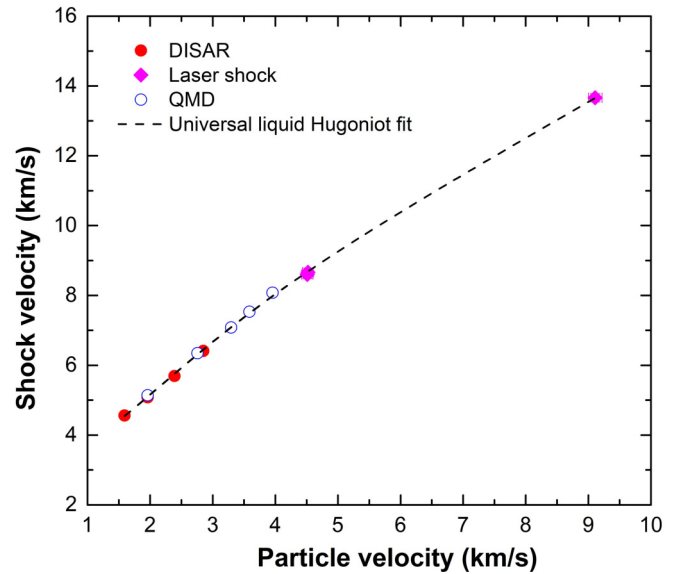| T (K)	$\rho(g/cm^3)$	P (GPa)
3 000	12.63	78.66
6 000	13.83	136.62
9 000	14.61	182.11
12 000	14.93	211.10
15 000	15.32	249.39

FIG. 6. Hugoniot data of PbF_2 in liquid-phase region. The dashed line is the result of fitting to Eq. (2).

version of the universal liquid Hugoniot [41]

$$U_S = A + BU_P - CU_P\exp(-DU_P), \qquad (3)$$

is used here to fit the simulation and experimental results, with the resulting coefficients: $A = 4.34(29)$, $B = 1.02(3)$, $C = 3.79(30)$, and $D = 0.91(10)$. The fitted curve is displayed as a dashed line in Fig. 6. As described by Duwal *et al.*, Eq. (3) asymptotically approaches a linear U_s–U_p relation for a wide range of U_p [35].

C. Universal behavior of AX_2 compounds at ultrahigh shock pressure

For metals, melting normally induces no or extremely small discontinuity on the Hugoniot [42]. In Fig. 7, we plotted the U_S–U_P Hugoniots of selected AX_2 compounds including quartz [41,43], TiO_2 [35], CaF_2 [44], and PbF_2. The small arrows indicate where melting occurs. Unlike metals, the Hugoniot slope (S) of these compounds decreases clearly on melting. Ozaki *et al.* noticed that at sufficiently high pressures, the Hugoniots of certain metals converge to the universal Hugoniot of fluid metal (UHFM), e.g., $U_S = 5.8 + 1.2\,U_P$ [27]. The Hugoniots of specific strong crystals such as diamonds and sapphires lie above the UHFM, whereas the Hugoniot of a soft material deuterium is under the UHFM; however, these Hugoniots have a similar S of ∼1.2. For the AX_2 compounds, the Hugoniots of CaF_2 and SiO_2 approached the UHFM at $U_P > ∼ 9$ km/s and ∼12 km/s, respectively. The TiO_2 Hugoniot is marginally above the UHFM and that of PbF_2 is under the UHFM. The Hugoniots of both TiO_2 and PbF_2 can also be approximated by a straight line with $S = 1.2$ for $U_P > ∼ 7$ and ∼4 km/s, respectively, as denoted by the dashed lines in Fig. 6. Therefore, $S = 1.2$ is not only the limiting pressure Hugoniot slope for metals, but also for nonmetals including AX_2 compounds. The slope S reflects the compressibility of a material along the Hugoniot. AX_2 compounds normally undergo a series of solid-solid phase
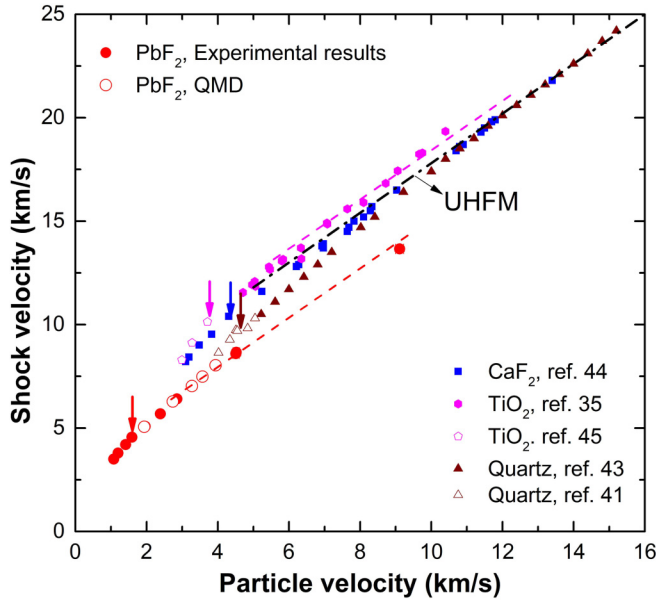
FIG. 7. U_s-U_p Hugoniot of specific AX_2 compounds. The dashed-dotted line is the UHFM ($U_s = 5.8 + 1.2\,U_p$). The dashed lines are linear fittings to the Hugoniot of TiO_2 and PbF_2 with S fixed at 1.2 for $U_p > 7\,\text{km/s}$ and $\sim 4\,\text{km/s}$, respectively. The small arrows indicate where melting occurs.

transitions before melting. Because the HP phase is less compressible than the LP phase, S increases with shock pressure. On melting, the Hugoniot softens and S decreases. At higher shock pressures, S further decreases and finally approaches ~ 1.2. The past shock compression studies on CaF_2 and BaF_2 detected a very stiff phase beyond ~ 100 GPa with $S = 1.7$ and 2.3, respectively [45,46]. Our study suggests that PbF_2 does not undergo such a phase change, consistent with a latest study on CaF_2 [44]. The Hugoniot of BaF_2 should be examined in the future.

V. CONCLUSIONS

Hugoniot data for PbF_2 single crystals were measured up to 1 TPa. Two phase transitions at ~ 29 and ~ 57 GPa were identified. Above 57 GPa, PbF_2 is in the fluid phase. The Hugoniot slope S of PbF_2 decreases upon melting and approaches the limiting pressure slope ($S = 1.2$) at higher shock pressures. The current study, combined with those on TiO_2, SiO_2, and CaF_2, suggest that for AX_2 compounds: (i) decreasing of S can be considered as an indication of melting and (ii) S approaches 1.2 at ultrahigh pressure, similar to that of metals. The Hugoniot data for AX_2 compounds at high pressure remain limited, and more study is required to confirm these conclusions.

One purpose of the present study was to search for a high-impedance window material that could remain transparent
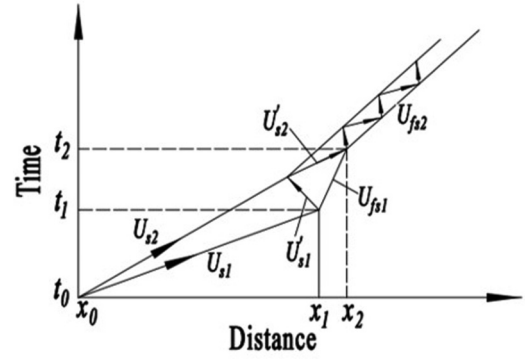
under strong shock compression. PbF_2 melts and becomes opaque at comparably low shock pressures. Finding a high-impedance window material remains a major challenge. The impedance of PbF_2 is comparable to that of sapphire, and its shock temperature is high, which benefits its application as an optical analyzer for measuring the sound velocity of shocked metals [47].

APPENDIX A

In the case of a two-wave structure, when the first shock wave reaches the free surface, it produces a rarefaction wave that propagates in the opposite direction. The rarefaction wave interacts with the oncoming second shock wave, reducing its intensity, as shown in Fig. 8. The velocity of the first shock wave is calculated by

FIG. 8. x–t diagram illustrating wave interactions in the IM experiments.

$$U_{s1} = \frac{x_1 - x_0}{t_1 - t_0} = \frac{H}{t_1 - t_0}, \tag{A1}$$

where H is the sample thickness and the corresponding particle velocity is obtained by the free-surface approximation, $U_{p1} = U_{fs1} / 2$. If the perturbation is ignored, the apparent shock velocity of the second wave is calculated by [48]

$$\bar{U}_{s2} = \frac{H + U_{fs1}(t_2 - t_1)}{t_2 - t_0}. \tag{A2}$$

In the above equations, t_0, t_1, and t_2 are arrival times as indicated in Fig. 1(a). The *true* second-shock velocity is given by

$$U_{s2} = \frac{U'_{s1}\bar{U}_{s2}(U_{s1} - U_{fs1}) + U_{s1}U'_{s2}(\bar{U}_{s2} - U_{fs1}) - U'_{s1}U'_{s2}(U_{s1} - \bar{U}_{s2})}{U'_{s2}(U_{s1} - U_{fs1}) + U'_{s1}(\bar{U}_{s2} - U_{fs1}) - U_{fs1}(U_{s1} - \bar{U}_{s2})}, \tag{A3}$$

TABLE V. Hugoniot data of PbF_2 in two-wave region with and without correction. U_p U_s, ρ, and P are the particle velocity, shock velocity, density, and Hugoniot pressure, respectively. Subscript 2 represents the second shock wave. The short bars above the symbol mean uncorrected data.

No.	$\bar{U}_{p2}$ (km/s)	$\bar{U}_{s2}$ (km/s)	$\bar{\rho}_2$ (g/cm^3)	$\bar{P}_2$ (GPa)	U_{p2} (km/s)	U_{s2} (km/s)	ρ_2 (g/cm^3)	P_2 (GPa)
1	0.75(1)	3.05(1)	10.16(5)	18.1(3)	0.75(1)	2.96(1)	10.27(5)	17.9(3)
2	0.91(1)	3.27(1)	10.67(5)	23.4(3)	0.91(1)	3.23(1)	10.72(5)	23.2(3)
3	1.08(1)	3.50(1)	11.17(5)	29.4(3)	1.08(1)	3.49(1)	11.19(5)	29.3(3)

where U'_{s1} and U'_{s2} are approximated by $U'_{s1} = U_{s1} - U_{p1}$ and $U'_{s2} = U_{s1} + U_{fs1}$. The particle velocity of the second shock wave U_{p2} is then calculated by impedance match between the driver plate and sample. For shots No. 1–3, the calculated Hugoniot data with and without corrections are listed in Table V.

APPENDIX B

Shock compression produces a quasiuniaxial strain state. The elastic shock response of a material can be calculated based on the nonlinear elastic theory. The stress along the shock direction is calculated as in Ref. [49],

$$\sigma_x = \frac{\rho_0}{\rho}\left(C_{xx}\eta + \frac{1}{2}C_{xxx}\eta^2\right), \tag{B1}$$

where ρ_0 is the initial density, ρ is the density under compression, $\eta = 0.5[(\rho_0 / \rho)^2 - 1]$, and is the Lagrangian strain. C_{xx} and C_{xxx} are the second- and third-order elastic constants along the shock direction, respectively. For PbF_2, the second- and third-order elastic constants were determined in previous works [18,50].

[1] G. A. Samara, Ferroelectrics **17**, 357 (1977).

[2] M. Nizam and Y. Bouteiller, J. Mol. Struct. **206**, 99 (1990).

[3] G. A. Samara, J. Phys. Chem. Solids **40**, 509 (1979).

[4] H. E. Lorenzana, J. E. Klepeis, M. J. Lipp, W. J. Evans, H. B. Radousky, and M. van Schilfgaarde, Phys. Rev. B **56**, 543 (1997).

[5] J. Haines, J. M. Léger, and O. Schulte, Phys. Rev. B **57**, 7551 (1998).

[6] A. Costales, M. A. Blanco, R. Pandey, and J. M. Recio, Phys. Rev. B **61**, 11359 (2000).

[7] C. V. Stan, R. Dutta, C. E. White, V. Prakapenka, and T. S. Duffy, Phys. Rev. B **94**, 024104 (2016).

[8] S. M. Dorfman, F. Jiang, Z. Mao, A. Kubo, Y. Meng, V. B. Prakapenka, and T. S. Duffy, Phys. Rev. B **81**, 174121 (2010).

[9] J. Oberschmidt and D. Lazarus, Phys. Rev. B **21**, 2952 (1980).

[10] A. R. Oganov, M. J. Gillan, and G. D. Price, Phys. Rev. B **71**, 064104 (2005).

[11] L. S. Dubrovinsky, N. A. Dubrovinskaia, V. Swamy, J. Muscat, N. M. Harrison, R. Ahuja, B. Holm, and B. Johansson, Nature (London) **410**, 653 (2001).

[12] S. R. Shieh, A. Kubo, T. S. Duffy, V. B. Prakapenka, and G. Shen, Phys. Rev. B **73**, 014105 (2006).

[13] J. Haines, J. M. Leger, and O. Schulte, J. Phys.: Condens. Matter **8**, 1631 (1996).

[14] S. Desgreniers and K. Lagarec, Phys. Rev. B **59**, 8467 (1999).

[15] O. Ohtaka, H. Fukui, T. Kunisada, T. Fujisawa, K. Funakoshi, W. Utsumi, T. Irifune, K. Kuroda, and T. Kikegawa, Phys. Rev. B **63**, 174108 (2001).

[16] H. X. Song, L. Liu, H. Y. Geng, and Q. Wu, Phys. Rev. B **87**, 184103 (2013).

[17] X. Liu, T. Mashimo, N. Kawai, T. Sekine, Z. Zeng, and X. Zhou, Mater. Res. Express **3**, 076206 (2016).

[18] J. C. Jamieson, M. H. Manghnani, T. Matsui, and L. C. Ming, J. Geophys. Res. **91**, 4643 (1986).

[19] P. A. Popov, A. A. Sidorov, E. A. Kul'chenkov, A. M. Anishchenko, I. Ch. Avetissov, N. I. Sorokin, and P. P. Fedorov, Ionics **23**, 233 (2017).

[20] T. Mashimo, Y. Zhang, M. Uchino, and A. Nakamura, Jpn. J. Appl. Phys. **48**, 096506 (2009).

[21] T. Mashimo, S. Ozaki, and K. Nagayama, Rev. Sci. Instrum. **55**, 226 (1984).

[22] T. Mashimo, X. Liu, M. Kodama, E. Zaretsky, M. Katayama, and K. Nagayama, J. Appl. Phys. **119**, 035904 (2016).

[23] J. D. Weng, H. Tan, X. Wang, Y. Ma, S. L. Hu, and X. S. Wang, Appl. Phys. Lett. **89**, 111101 (2006).

[24] X. Hu, G. Yang, B. Zhao, P. Li, J. Yang, C. Leng, H. Liu, H. Huang, and Y. Fei, J. Appl. Phys. **123**, 175903 (2018).

[25] A. C. Mitchell and W. J. Nellis, J. Appl. Phys. **52**, 3363 (1981).

[26] N. Ozaki, T. Sano, M. Ikoma, K. Shigemori, T. Kimura, K. Miyanishi, T. Vinci, F. H. Ree, H. Azechi, T. Endo, Y. Hironaka, Y. Hori, A. Iwamoto, T. Kadono, H. Nagatomo, M. Nakai, T. Norimatsu, T. Okuchi, K. Otani, T. Sakaiya, K. Shimizu, A. Shiroshita, A. Sunahara, H. Takahashi, and R. Kodama, Phys. Plasmas **16**, 062702 (2009).

[27] N. Ozaki, W. J. Nellis, T. Mashimo, M. Ramzan, R. Ahuja, T. Kaewmaraya, T. Kimura, M. Knudson, K. Miyanishi, Y. Sakawa, T. Sano, and R. Kodama, Sci. Rep. **6**, 26000 (2016).

[28] P. M. Celliers, D. K. Bradley, G. W. Collins, D. G. Hicks, T. R. Boehly, and W. J. Armstrong, Rev. Sci. Instrum. **75**, 4916 (2004).

[29] J. W. Forbes, *Shock Wave Compression of Condensed Materr-A Primer* (Springer, Berlin, 2012), pp. 17, 45.

[30] M. D. Knudson and M. P. Desjarlais, Phys. Rev. B **88**, 184107 (2013).

[31] M. D. Knudson, M. P. Desjarlais, and A. Pribram-Jones, Phys. Rev. B **91**, 224105 (2015).

[32] W. J. Nellis, A. C. Mitchell, and A. C. Young, J. Appl. Phys. **93**, 304 (2003).

[33] X. Cao, Y. Wang, X. Li, L. Xu, L. Liu, Y. Yu, R. Qin, W. Zhu, S. Tang, L. He, C. Meng, B. Zhang, and X. Peng, J. Appl. Phys. **121**, 115903 (2017).

[34] http://www.quantum-espresso.org/

[35] S. Duwal, C. A. McCoy, P. F. Weck, P. Kalita, H. L. Hanshaw, K. Cochrane, T. Ao, and S. Root, Phys. Rev. B **102**, 024105 (2020).

[36] J. P. Perdew, K. Burke, and M. Ernzerhof, Phys. Rev. Lett. **77**, 3865 (1996).

[37] J. P. Perdew, J. A. Chevary, S. H. Vosko, K. A. Jackson, M. R. Pederson, D. J. Singh, and C. Fiolhais, Phys. Rev. B **46**, 6671 (1992).

[38] D. R. Hamann, Phys. Rev. B **88**, 085117 (2013).

[39] X. M. Zhou, J. Li, W. J. Nellis, X. Wang, J. B. Li, H. L. He, and Q. Wu, J. Appl. Phys. **109**, 083536 (2011).

[40] Z. P. Tang and Y. M. Gupta, J. Appl. Phys. **81**, 7203 (1997).

[41] M. D. Knudson and M. P. Desjarlais, Phys. Rev. Lett. **103**, 225501 (2009).

[42] S. P. Marsh, *LASL Shock Hugoniot Data* (University of California Press, Los Angeles, 1980).

[43] G. A. Lyzenga, Shock temperatures of materials: Experiments and application to the high pressure equation of state, Ph.D. thesis, California Institute of Technology, 1980.

[44] S. Root, M. Desjarlais, R. Lemke, P. Kalita, and S. Alexander, Sandia Report No. SAND2018-0182C (2018).

[45] L. V. Al'tshuler, M. A. Podurets, G. V. Simakov, and R. F. Trunin, Fiz. Tverd. Tela **15**, 1436 (1973) [Sov. Phys. Solid State **15**, 969 (1973)].

[46] R. F. Trunin, L. F. Gudarenko, M. V. Zhernokletov, and G. V. Simakov, *Experimental Data on Shock Compressibility and Adiabatic Expansion of Condensed Substances* (RFNC-VNIIEF, Sarov, Russia, 2001).

[47] J. M. Brown and R. G. McQueen, J. Geophys. Res. **91**, 7485 (1986).

[48] W. H. Gust and E. B. Roye, J. Appl. Phys. **42**, 276 (1971).

[49] J. M. Lang and Y. M. Gupta, Phys. Rev. Lett. **106**, 125502 (2011).

[50] J. Shanker and J. P. Singh, Phys. Status Solidi B **110**, 697 (1982).